https://doi.org/10.5194/egusphere-2026-5477
Preprint. Discussion started: 22 September 2026

Quantifying Long-Term Ground Surface Subsidence in the Lena Delta Induced by Degrading Permafrost Using Sentinel-1 SAR Interferometry

Tazio Strozzi[1], Barbara Widhalm[2], Nina Jones[1], Julia Boike[3,4], Sofia Antonova[3], Birgit Heim[3], Sebastian Westermann[5], Andreas Kääb[5], Annett Bartsch[2]

[1]Gamma Remote Sensing, Gümligen, 3073, Switzerland
[2]b.geos GmbH, Korneuburg, 2100, Austria
[3]Alfred Wegener Institute Helmholtz Centre for Polar and Marine Research, Potsdam, 14473, Germany
[4]Humboldt University, Geography Department, Berlin, 10099, Germany
[5]Department of Geosciences, University of Oslo, Oslo, 0316, Norway

Correspondence to: Tazio Strozzi (strozzi@gamma-rs.ch)

Abstract. Recent atmospheric warming has led to widespread permafrost degradation and subsidence induced by ground ice thaw across the pan-Arctic permafrost domain of North America and Eurasia. Reported subsidence rates reach up to 2 cm/year in areas with low ice content and exceed 3 cm/year in ice-rich regions. Quantifying long-term subsidence trends over extensive areas is critically important to detect and assess permafrost changes and impacts. Unlike the development of localized thermokarst features, the isotropic thaw subsidence is relatively slow and spatially more uniform across broad spatial scales. Consequently, long-term monitoring at numerous sites and over large areas is essential for understanding the impacts of permafrost thaw and for improving numerical simulations of permafrost degradation and ground surface subsidence. Here, we show that Sentinel-1 SAR interferometry can be successfully used to monitor long-term surface subsidence rates in the Lena Delta in northeastern Siberia. The observed ground surface subsidence rates between 2016 and 2021 vary significantly among the three geomorphological units of the Lena Delta and turn out to be closely linked to ground ice content. The largest subsidence rate, at 16.0 ± 7.2 mm/year, occurs in the Yedoma, the most ground-ice rich geomorphological unit. In contrast, the most stable geomorphological unit, with subsidence rates of 1.0 ± 4.4 mm/year, is associated with a predominantly sand-dominated lithology having low ground-ice content and dry vegetation cover. The youngest and most active part of the delta, consisting of Holocene river terraces with polygonal tundra and the present-day floodplains, is characterized by heterogeneous subsidence rates of 7.0 ± 5.3 mm/year. For continuous monitoring of long-term ground surface subsidence over larger Arctic regions using Sentinel-1 data, a long series of satellite acquisitions with preserved long-term coherence (e.g., over one year of summer acquisitions) is required. While Sentinel-1 C-band data suffer from poor coherence over one-year intervals, SAR systems with longer wavelengths (e.g., L-band) can achieve better performance for this purpose.

https://doi.org/10.5194/egusphere-2026-5477
Preprint. Discussion started: 22 September 2026

1 Introduction

Permafrost is defined as ground that remains at or below 0°C for two or more consecutive years. It underlies large areas of the Arctic. Recognizing its importance as a climate indicator, the Global Climate Observing System (GCOS) has designated permafrost as an Essential Climate Variable (ECV), with three associated quantities: ground temperature (GT), active layer thickness (ALT), and rock glacier velocity (RGV). The active layer is defined as the ground that seasonally thaws and refreezes above the permafrost table. In moist polar environments, the transition zone between the active layer and the permafrost table often contains a high proportion of interstitial ice, forming an ice-rich layer several centimeters to decimeters thick (Farzamian et al., 2020). The enrichment or degradation of ice within this transition layer—through the formation or melting of ice lenses at the base of the active layer—together with volumetric changes caused by ice formation and melt in the active layer and redistribution of water after ice thaw, seasonally manifests as ground surface heave or subsidence, respectively. If, over the long term, lowering of the summer ground surface exceeds winter heaving, net subsidence results. Owing to atmospheric warming in recent years (Forster et al., 2023), permafrost degradation has been widely reported (Grosse et al., 2011), with consequences including coastal retreat, infrastructure instability, thermokarst development, and carbon dioxide (CO_2) and methane (CH_4) emissions. Quantifying the long-term subsidence trend across extensive areas is of critical importance to assess and understand permafrost changes.

Streletskiy et al. (2025) provided a comprehensive overview of methods for observing and modeling vertical ground surface displacement and analyzed publicly available data. Based on field observations, remote sensing, and numerical modeling, the authors confirmed widespread thaw subsidence across the pan-Arctic permafrost domain in North America and Eurasia, with rates of up to 2 cm/year in low-ice-content areas and exceeding 3 cm/year in ice-rich regions. Beforehand, Shiklomanov et al. (2013) presented an 11-year high-resolution record of temperature and in-situ vertical ground surface movement obtained using differential Global Positioning System (GPS) across contrasting physiographic regions in northern Alaska. They found that thawing of the ice-rich layer at the top of the permafrost produced decimeter-scale subsidence extending across the entire landscape during this period. Similarly, O'Neill et al. (2023) documented widespread permafrost thaw and ground surface subsidence using thaw tube measurements across a large portion of northwest Canada. Measured relative to a fixed datum, thawing amounted to approximately 22 cm over three decades. Shiklomanov et al. (2013) and O'Neill et al. (2023) further noted that ALT measurements referenced to the ground surface systematically underestimate thaw in ice-rich permafrost due to subsidence-induced datum lowering. In the context of permafrost degradation induced by climate change, the net melting of ground ice at the base of the active layer represents an important thaw trajectory that is not captured by the current ECV quantities GT and ALT.

Taken together, the results summarized above suggest that the entire natural landscape underlain by ice-rich permafrost may be slowly subsiding in response to atmospheric warming. Compared with the development of many local thermokarst features, this isotropic thaw subsidence is relatively slow (decimeters per decade) and geographically uniform, but scales with waste areas. Nevertheless, predicting permafrost degradation and ground surface subsidence over large areas using

https://doi.org/10.5194/egusphere-2026-5477
Preprint. Discussion started: 22 September 2026

numerical simulations remains challenging (Aga et al., 2023; Westermann et al., 2025). This difficulty arises because key environmental controls—including vegetation type, soil wetness, snow cover dynamics, and ground ice content—can vary substantially over short distances, each exerting a strong influence on local thaw and subsidence rates. Consequently, long-term monitoring of these variables at numerous sites is essential for understanding the impacts of climate change on permafrost thaw. Local site conditions, such as those observed in ice-rich areas (Fedorov et al., 2022), can change markedly within short spatial distances, further underscoring the need for high-resolution observational networks. Remote sensing offers a key approach to addressing this challenge, enabling systematic, and spatially extensive documentation of surface displacement across otherwise inaccessible permafrost regions.

Satellite synthetic aperture radar differential interferometry (DInSAR) enables large-scale assessment of seasonal and long-term ground surface displacement (e.g., Liu et al., 2010; Short et al., 2011; Liu et al., 2012; Strozzi et al., 2018; Rouyet et al., 2019; Zwieback et al., 2024; Widhalm et al., 2025). In particular, the availability of Sentinel-1 C-band time series data from 2014 onward has facilitated comprehensive analyses of both seasonal and long-term deformation across diverse Arctic permafrost landscapes (Bartsch et al., 2026). In these settings, seasonal deformation patterns – primarily sensitive to active layer ground ice content (Wendt et al., 2026) – have been found to differ from long-term subsidence patterns, with the latter mainly reflecting the melt of excess ground ice (Zwieback et al., 2024; Bartsch et al., 2026). We build upon this research with a study focused on the Lena Delta, a biodiversity hotspot and natural reserve in northeastern Siberia. Although Holocene floodplain sediments rich in ground ice are widespread in Arctic deltas, long-term subsidence within such ice-rich deposits remains less frequently described or modelled than lithospheric subsidence driven by sedimentary loading (Walker, 1998). Seasonal vertical surface thaw displacement on Samoylov Island has previously been measured using satellite SAR interferometry with X-, C-, and L-band sensors (Strozzi et al., 2026). Here, we quantify long-term subsidence driven by permafrost degradation using Sentinel-1 data acquired between 2016 and 2021 over the broader Lena Delta region. We then compare these satellite-based estimates with in-situ measurements to evaluate the reliability of DInSAR-derived deformation signals as proxies for permafrost thaw.

2 Study site

The Lena Delta is located in the High Arctic Zone of northeastern Siberia, on the coast of the Laptev Sea. It constitutes the largest river delta in the Arctic, covering an area of around 32’000 km2 between 72° and 74° N (Are and Reimnitz, 2000). The Lena Delta is dominated by continuous permafrost in a continental climate (Obu et al., 2019; Westermann et al., 2025), with extremely cold winter and relatively warm summer temperatures (Boike et al., 2013). Mean annual ground temperatures are on the order of -12° C and the frozen ground is estimated to extend to a depth of about 400–600 m below the surface (Boike et al., 2019). Figure 1 shows a map of the habitat classes observed in the Lena Delta (Lisovski et al., 2023). Based on extensive knowledge collected during fieldwork and hyperspectral field measurements combined with Sentinel-2 satellite data, 11 distinct habitat classes associated to different vegetation compositions were defined. The surface and ground

https://doi.org/10.5194/egusphere-2026-5477
Preprint. Discussion started: 22 September 2026

properties of the Lena Delta feature a strong heterogeneity at spatial scales of 1 m to 1 km, with, for example, a large number of small water bodies. Despite such small-scale variability, the Lena Delta can be classified in three main geomorphological units, also referred to as terraces, which have distinctly different characteristics regarding their surface and subsurface properties, such as ground ice contents, thermokarst features and vegetation cover (Grigoriev 1993, Schwamborn et al., 2002; Morgenstern et al., 2011; Morgenstern et al., 2013; Westermann et al., 2017). This difference in ice contents and textures is also reflected in the maps of ground ice content and cryogenic processes (Shestakova et al., 2021) and in the map of the land cover diversity considering wetness gradients (Bartsch et al., 2024), presented in Appendix A. Note that here we use the term habitat class instead of land cover class – a term which, whilst essentially synonymous, is more common – to highlight the distinction between the Lisovski et al. (2023) habitat map from the Bartsch et al. (2024) land cover units.

The youngest geomorphological unit occupies the eastern and central Lena Delta, accounting for nearly 65% of its total area (Lisovski et al., 2023). It is the most active part of the delta, built up by active sandy floodplains shaped by river erosion and sedimentation and Holocene river terraces with ice-rich polygonal tundra. A considerable fraction of this geomorphological unit is composed of the modern floodplain of the Lena River, which is periodically inundated resulting in a mosaic of sand flats, shrublands and wetlands, and wet to aquatic tundra land-cover units (Bartsch et al., 2024). These floodplain areas feature a subsurface stratigraphy with sandy, generally well-drained soils. In the less vegetated areas, these soils have low organic contents. In the wetland parts, they consist of fine-grained, poorly drained deeper soils (Lisovski et al., 2023). Mineral and organic ice contents reach 20–40 % and 5–10 %, respectively (Westermann et al., 2017). The surface of the Holocene part of this geomorphological unit is dominated by polygonal tundra with up to 20 % surface water in the form of thaw ponds and larger lakes and tundra with mosses, sedges, grass, and occasional dwarf shrubs (Boike et al., 2013, Lisovski et al., 2023) (Figure 2). Here, the subsurface material consists of silty sands and organic matter in alluvial peat layers with thicknesses up to 5–6 m (Grigoriev, 1993; Schwamborn et al., 2002). Ice wedges of more than 9 m depth have been described on the Holocene terraces and the ice contents in the uppermost few meters reach up to 60–80% in volume (Westermann et al., 2017). In contrast, the ice content maps of Shestakova et al. (2021) show values of only 20–40% (Appendix A1a and A2a) – substantially lower than those for the other geomorphological units. This discrepancy likely arises because the ice content maps represent average ice content across larger areas, whereas the 60–80% values correspond specifically to ice-wedge-rich zones. With respect to the cryogenic processes, the youngest geomorphological unit shows a combination of frost cracking, thermokarst and frost heaving (Appendix A1b and A2b) (Shestakova et al., 2021).

The second geomorphological unit, located in the northwestern part of the Lena Delta, consists of non-deltaic units of Late Pleistocene to early Holocene sandy sediments deposited between 30 and 15 ka BP, when the sea level was lower than today. The Pleistocene sand-dominated unit covers about 27% of the area. These sandy sediments generally feature low ice and organic contents (Westermann et al., 2017). The ice content of this unit is also indicated to be mostly low values in the map by Shestakova et al. (2021), comparable to those of the youngest geomorphological unit, with localized patches reaching slightly higher values of 40–60 % (Appendix A1a and A2a). In most parts of this unit frost cracking is the most dominant cryogenic process (Shestakova et al., 2021) (Appendix A1b and A2b). The Pleistocene sandy geomorphological unit is

https://doi.org/10.5194/egusphere-2026-5477
Preprint. Discussion started: 22 September 2026

mostly characterized by dry to moist tundra (Bartsch et al., 2024) (Appendix A1c and A2c), with the most common habitat classes being dry dwarf shrub and herb communities, typically very dry and low in biomass, along with polygonal tundra in the thermokarst basins (Lisovski et al., 2023) (Figure 2).

The third geomorphological unit is composed of Late-Pleistocene, ice-rich Yedoma-type ice complexes accumulated during the extremely cold climate of the last glacial period between 43 and 14 ka BP. It is distributed in several large islands in the southern margins of the Lena Delta, accounting for roughly 8% of its total area. The Yedoma unit contains substantial quantities of ground ice and organic carbon down to several tens of meters below the surface, with ice wedges of more than 25 m depth and several meters wide (Grigoriev, 1993; Morgenstern et al., 2011; Schirrmeister et al., 2011; Morgenstern et al., 2013). Ground ice content is also mapped in Shestakova et al. (2021) as the highest for the Lena Delta, with mostly 60-80 % (Appendix A1a and A2a). The most common habitat classes on the Yedoma unit are polygonal tundra with up to 10 % surface water mostly in the form of thermokarst ponds, and dry tussock tundra communities (Lisovski et al., 2023) (Figure 2). The vegetation consists of thick 0.1–0.2 m hummocky grass, sedge and moss cover, and the upper horizon of the soil has a thick organic layer (Antonova et al., 2017). Holocene permafrost degradation resulted in the current complex thermokarst landscape, where thermokarst represents the prevailing cryogenic process (Shestakova et al., 2021) (Appendix A1b and A2b), characterized by thermokarst lakes and drained basins (Morgenstern et al., 2011; Morgenstern et al., 2013).

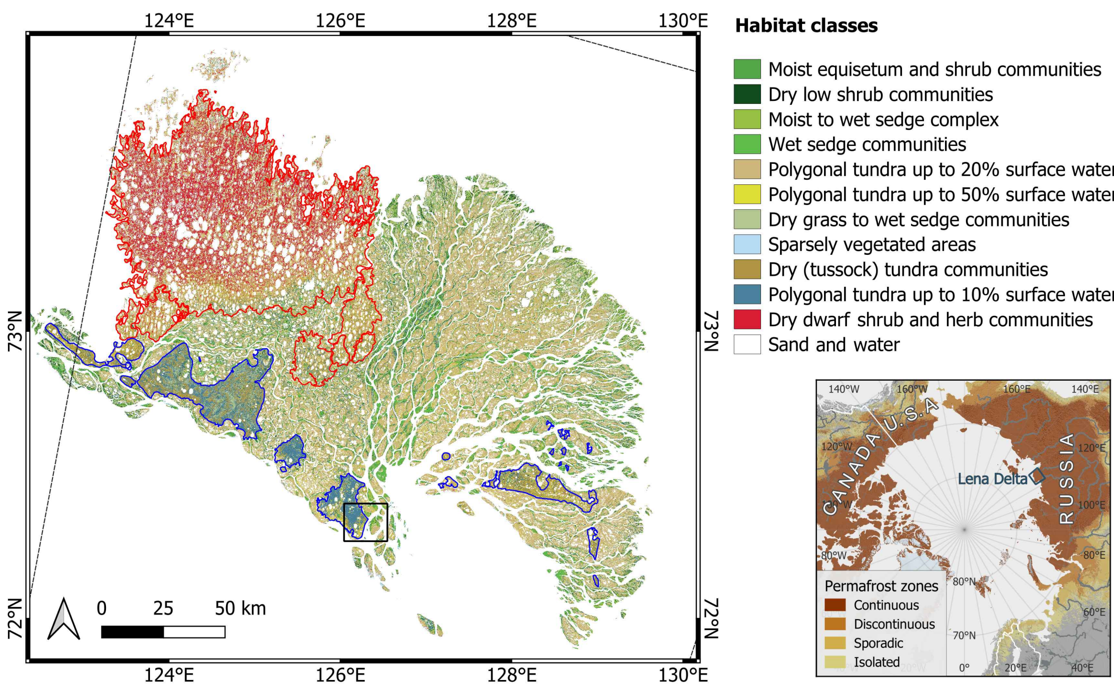

Figure 1: Habitat classes of the Lena Delta (Lisovski et al., 2023) with extension of the sand-dominated geomorphological unit in red and of the Yedoma geomorphological unit in blue. The remaining areas represent the youngest geomorphological unit, with Holocene terraces and the modern floodplains. The footprint of the Sentinel-1 images is shown with a dashed black line. The black rectangle shows the location of the islands of Kurungnakh-Sise and Samoylov (see Figure 5). The bottom right inset shows an overview map with the permafrost zonation in the Arctic after Westermann et al. (2025) with the location of the Lena Delta region.

https://doi.org/10.5194/egusphere-2026-5477
Preprint. Discussion started: 22 September 2026

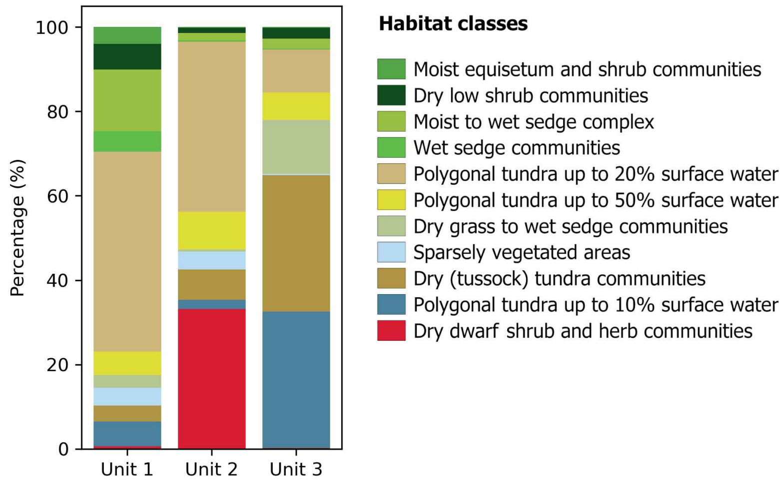

Figure 2. Bar plot showing the proportion of habitat classes within the three geomorphological units of the Lena Delta: Unit 1 is the youngest one with Holocene terraces and modern floodplains, Unit 2 is the Pleistocene sand-dominated one, and Unit 3 is the Yedoma one.

3 Data and methods

3.1 Satellite synthetic aperture radar differential interferometry (DInSAR)

To derive the long-term vertical displacement rate over the Lena Delta, we apply advanced differential interferometric synthetic aperture radar techniques (DInSAR) using C-band Sentinel-1 data. Following a baseline, pre-defined mission observation scenario (Torres et al., 2012), Sentinel-1 commonly acquired SAR images in the Interferometric Wide (IW) swath mode every 12 days between July 2016 until December 2021 over the region of interest. The Sentinel-1 frame is 250 km wide (Figure 1), the spatial resolution is 5 m in slant-range and 20 m azimuth and the incidence angle is 38º at the center of the frame. The phase difference between two such acquisitions can be measured with DInSAR and converted to displacement (Bamler and Hartl, 1998, Rosen et al., 2000). The processing sequence is based on Single Look Complex (SLC) data acquired between June and September of each year – a snow-free time window – from 2016 to 2021 (Supplementary Table B1). First, a reference SLC is selected and geocoded to the TanDEM-X digital elevation model (DEM). The TanDEM-X DEM is based on satellite TanDEM-X SAR acquisitions from December 2010 to early 2015 and the product is provided with a pixel spacing of approximately 12 m (Zink and Moreira, 2014). GPS comparisons prove an absolute vertical mean error of the TanDEM-X DEM smaller than ±0.20 m, a root mean square error (RMSE) smaller than 1.4 m (±1.1 m for low vegetation) and an absolute 90% linear height error below 2 m (Wessel et al., 2018). All other SLC images are then coregistered to the reference image. From these, we generate differential interferograms with a multi-looking factor of 5 pixels in slant-range and of 1 pixel in azimuth of 12 to 36 days for each summer and link them with few differential interferograms of 1-year temporal baselines to bridge the winter seasons (Supplementary Figure B1). After removal of the topographic phase component through use of the available TanDEM-X DEM, the phase difference of each

https://doi.org/10.5194/egusphere-2026-5477
Preprint. Discussion started: 22 September 2026

pair reflects surface movement in the satellite line-of-sight (LOS) as phase cycles of a 2π ambiguity in wrapped differential interferograms, with atmospheric disturbances as the major limitation. Random errors in the differential interferograms are removed with adaptive filtering based on the power spectral density (Goldstein and Werner, 1998), while noisy and decorrelated areas are masked out based on a mean 12-day coherence threshold below 0.8 and on a mean filtered interferogram correlation coefficient below 0.6 (Strozzi et al., 2026). The coherence map of the Lena Delta (Supplementary Figure B2) shows the highest values over the sandy sediments and lowest values – which are, however, still above the thresholds – for the floodplain areas of the youngest geomorphological unit. Water in rivers and lakes lies below the coherence thresholds and is therefore masked out. To derive the absolute displacement in meters, phase unwrapping is applied with minimum cost flow procedures (Costantini, 1998) followed by a manual ambiguity correction based on a visual check of residues of phase unwrapping. The phase reference region is selected at 126.397°E, 72.317°N, in a relatively homogeneous polygonal tundra area with up to 50% surface water cover and high coherence. The resulting filtered and unwrapped differential interferograms are then inverted to derive phase time series of LOS displacement occurring from 22 July 2016 to 24 September 2021 (Berardino et al., 2002, Werner et al., 2012), from which the long-term displacement rate over Lena Delta in m/year is determined with a linear regression. Finally, the LOS displacement is converted to vertical displacement using the sensor incidence angle. Such an approximation is based on the assumption that ground surface displacement is predominantly in the vertical direction and is valid in flat areas devoid of significant topographic relief. With elevations between 0 and 60 m a.s.l., the Lena Delta can essentially be regarded as flat (Westermann et al., 2017). To derive the displacement time series, an additional low-frequency correction is applied to the residual phases (i.e. the phase time series with subtraction of the linear deformation rate) to smooth atmospheric noise across a radius of 2048 range samples, corresponding to approx. 40 km (Michaelides et al., 2021).

To calibrate the long-term displacement rate, several stationary locations – so called stable targets – are considered (Strozzi et al., 2026). Two locations in the central Lena Delta are elevated, barren bedrock exposures and are assumed to be stationary: Amerika Khaya (72.476 N 126.281 E) and Stolb Island (72.396 N 126.660 E). Additionally, we take into account three barren, exposed surfaces with rock rubble at 72.188 E 127.645 N, 72.405 N 126.860 E and 72.339 N 125.537 E along the southern margin on the mainland side, as well as the airport (71.706 N 128.898 E) and a flat-topped mountain (71.623 N 128.868 E) near Tiksi, the nearest settlement to the Lena Delta, located about 115 km to the southeast. We linearly adjust the long-term displacement rate so that, on average, it is zero at the seven locations considered stationary. After calibration the long-term displacement rate is 0.02 cm/year at Amerika Khaya, -0.01 cm/year at Stolb Island, 0.06 cm/year, 0.23 cm/year and 0.02 cm/year at the three barren exposed surfaces at the southern margin on the mainland side, -0.15 cm/year at the Tiksi airport runway and -0.17 cm/year at the flat-topped mountain near Tiksi. These values serve as a first rough indication of the product accuracy.

https://doi.org/10.5194/egusphere-2026-5477
Preprint. Discussion started: 22 September 2026

3.2 In-situ data

In-situ surface displacement was measured on Kurungnakh-Sise Island and on Samoylov Island in the southern part of the Lena Delta, see Figure 1 for location. Kurungnakh-Sise Island largely represents the remnants of a late Pleistocene accumulation plain and is part of the Yedoma unit. Stratigraphically, the island consists of 15–20 m thick fluvial silty sands overlain by up to 40 m thick ice-rich peaty and silty deposits. The ground ice in these deposits occurs in the form of small ice veins and lenses as well as giant ice wedges, which can reach up to 20 m high and several meters wide. Samoylov Island is situated in the youngest and most active part of the Lena Delta and is divided in two parts (Lisovski et al. 2023). The central and eastern part consists of a Holocene river terrace dominated by wet polygonal tundra. This area is characterised by low-centred ice-wedge polygons and reaches end-of-season thaw depths of about 0.5 m, with annual maxima between 42 and 57 cm (Boike et al., 2013). Grasses, hydrophytic sedges as well as mosses dominate the vegetation in the wet polygon centers and at their edges, while mesophytic dwarf shrubs and mosses dominate the polygon rims. The western part of Samoylov Island is part of the modern active floodplain of the Lena River, with large sand flats as well as ridges covered by shrubs and deeper wetland parts, that are annually flooded in spring (Heim et al., 2022).

Surface displacement was determined by repeatedly measuring the distance between the top of a steel pipe or fiberglass pole anchored in the permafrost, and a plexiglass plate resting on the ground surface (Antonova et al., 2018). Displacement is therefore relative to the surface, not to an external datum. On Kurungnakh-Sise Island, this method was applied to an array consisting of 12 steel pipes and 19 fiberglass poles. Measurements were taken twice per year, at the end of the snow covered season (April/May) and at the end of the thaw season (September), from April 2013 to September 2020, with a gap in 2015 and in in spring 2016. The long-term displacement rate was determined as the slope of these measurements. Surface displacement on Samoylov Island was measured exclusively on the Holocene river terrace part. Between one and eight measurements were taken per year, using three steel pipes from August 2013 to September 2020 and four fiberglass poles from September 2017 to September 2020 (seven points in total). Again, the long-term displacement rate was determined as the slope of these measurements. No subsidence measurement setup was possible in the western active floodplain part of the island.

The measurement setup and the sources of potential errors in the field measurements are described in detail in Antonova et al. (2018). We consider ±1 cm to be a conservative uncertainty estimate for each individual in-situ measurement. Since the long-term displacement rate is derived from the slope across multiple measurements, its uncertainty is smaller than that of a single measurement. However, this rate uncertainty is larger for the four Samoylov fiberglass poles, which have a shorter three-year record (2017–2020), than for the other points, which cover the period from 2013 to 2020. Additional sources of error could include: (i) snow and ice present on the surface during winter measurements, which may cause positive deformation; and (ii) upward movement of the steel pipe or fiberglass pole, which can subsequently produce large negative deformation values. Despite these potential sources of error, we did not exclude any ground-based measurement data from the analysis.

https://doi.org/10.5194/egusphere-2026-5477
Preprint. Discussion started: 22 September 2026

4 Results

4.1 Sentinel-1 long-term displacement rate

The long-term vertical displacement rate from Sentinel-1 data between 22 July 2016 and 24 September 2021 over the Lena Delta is presented in Figure 3. The color code is saturated at +1 cm/year for heave and −2 cm/year for subsidence, where red indicates positive (upward) displacement and blue indicates negative (downward) displacement. The highest deformation rates are observed over the Yedoma geomorphological unit, whereas a more stable region is found over the Pleistocene sand-dominated geomorphological unit. The youngest geomorphological unit is characterized by heterogeneous rates of motion, depending on the lithology linked to the Holocene river terraces or to the wetland parts of the modern floodplains. Quantitatively, over the youngest unit the mean long-term vertical displacement rate is -7.0 mm/year with a standard deviation, representing the spatial variability of subsidence within this unit, of 5.3 mm/year. Over the Pleistocene sand-dominated unit, the mean is -1.0 mm/year with a standard deviation of 4.4 mm/year. Over the Yedoma unit, the mean rate is -16.0 mm/year with a standard deviation of 7.2 mm/year. The slight heave apparent in some areas (red in Figure 3), especially over sand-dominated units, is elaborated in the discussion section below.

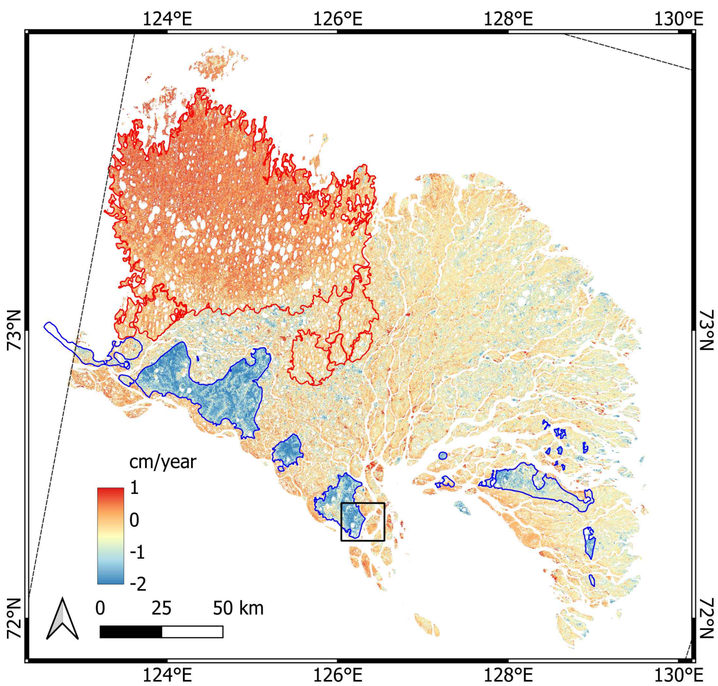

Figure 3: Long-term displacement rate from Sentinel-1 data between 22 July 2016 and 24 September 2021 over the Lena Delta. The region of interest corresponds to that of the map of the habitat classes (Figure 1), i.e. sand and water in white are masked out. The extent of the sand-dominated geomorphological unit is marked by red outlines and that of the Yedoma geomorphological unit by blue outlines; the remaining areas are the youngest geomorphological unit, with Holocene terraces and modern floodplains. The footprint of the Sentinel-1 images is shown with a dashed black line. The black rectangle shows the location of the islands of Kurungnakh-Sise and Samoylov (see Figure 4).

https://doi.org/10.5194/egusphere-2026-5477
Preprint. Discussion started: 22 September 2026

Time series of displacement for four locations between Kurungnakh-Sise Island and Samoylov Island in the southern part of the Lena Delta are shown in Figure 4. Because we considered in our analysis only coherent interferograms available during the snow-free period from June to September of each year, the time series cannot display the full annual history of displacement. For regions with both a high and low long-term displacement rate there are areas characterized by prominent seasonal thaw displacement (i.e., Points 1 and 3) and areas without distinctive seasonal deformation (i.e., Points 2 and 4). For regions with a high long-term displacement rate (i.e., Points 1 and 2), the time series might point to accelerating subsidence after 2018, when the air temperature showed a significant rise. According to temperature records measured on Samoylov Island (Boike et al., 2019), the Accumulated Thawing Degree Days (ATDD) – computed by summing the positive mean daily temperature over the course of the thawing season and often referred to as the thawing index or summer index – increased from 801ºC in 2016 and 700ºC in 2017 to 990ºC in 2018. Afterwards, the ATDD remained high at 1025ºC in 2019, 1128ºC in 2020 and 1108ºC in 2021. In general, however, the Sentinel-1 time series of displacement are not long and consistent enough over the years to conclusively display the effects of warmer years.

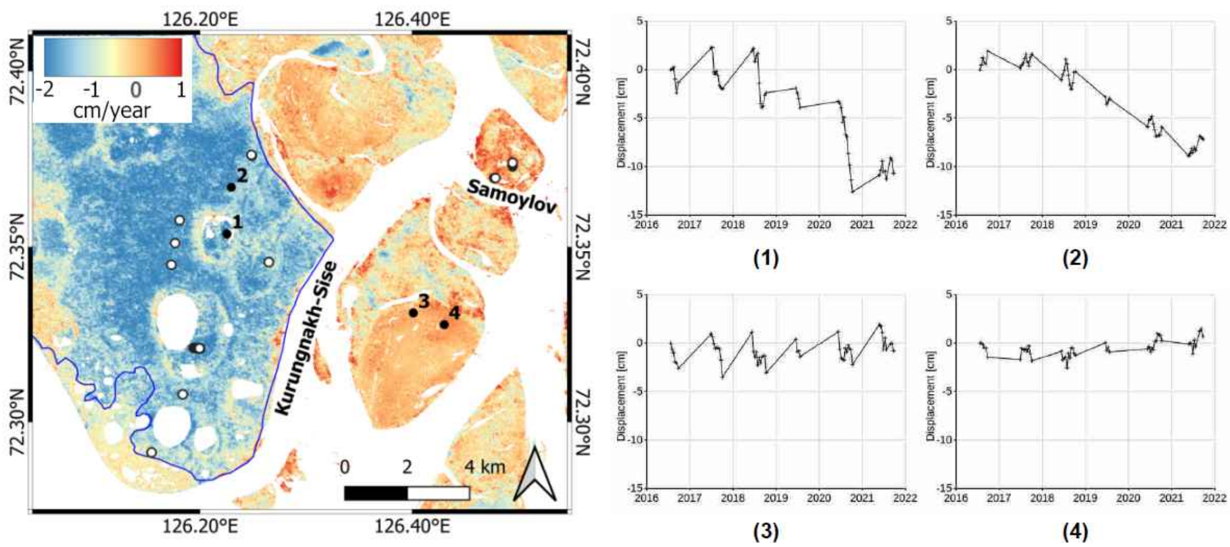

(a) (b)

Figure 4: Long-term displacement rate from Sentinel-1 data between 22 July 2016 and 24 September 2021 between Kurungnakh-Sise Island and Samoylov Island in the southern part of the Lena Delta. The extent of the Yedoma geomorphological unit lies within the blue outlines. White dots are the locations of in-situ surface displacement measurements on Kurungnakh-Sise Island in the west and on Samoylov Island in the east. (b) Time-series of DInSAR displacements for four selected points, for position see black dots on (a).

4.2 In-situ displacement rate

Figure 5 shows a scatter plot of the long-term displacement rates measured in-situ and derived by satellite over the islands of Kurungnakh-Sise and Samoylov. In-situ displacement rates were measured between 2013 and 2020 on all sites apart from the four fiberglass poles on Samoylov Island, which were installed 2017. Satellite displacement rates were derived for the

https://doi.org/10.5194/egusphere-2026-5477
Preprint. Discussion started: 22 September 2026

period 22 July 2016 to 24 September 2021. The in-situ and satellite records therefore cover offset periods, and for the four fiberglass poles on Samoylov Island the in-situ rate is based on only three years of data.

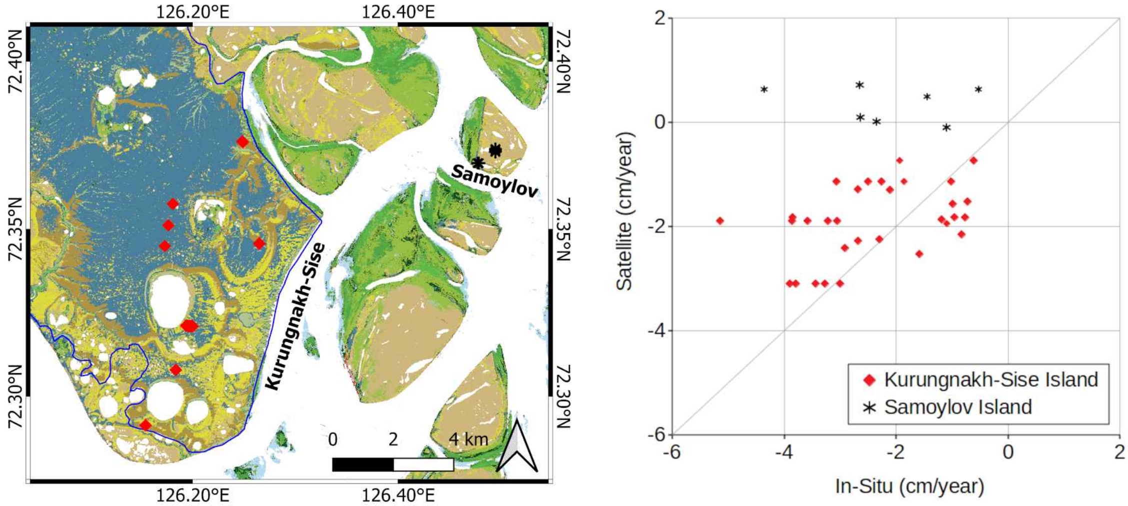

(a) (b)

Figure 5: (a) Habitat classes of the Lena Delta (Lisovski et al., 2023) with the extent of the Yedoma geomorphological unit shown within the blue outlines. Legend as in Figure 1. Red diamonds and black stars are the locations of in-situ surface displacement measurements on Kurungnakh-Sise Island in the west and Samoylov Island in the east, respectively. (b) Scatter plot of in-situ versus satellite estimated long-term displacement rate (n = 31 on Kurungnakh-Sise Island, n = 7 on Samoylov Island). In-situ displacement was measured between 2013 and 2020 on all sites apart from the four fiberglass poles on Samoylov Island which were installed in 2017 and cover 2017–2020 only. The satellite displacement rate was derived between 22 July 2016 and 24 September 2021. Negative values denote subsidence.

For the in-situ monitoring points on Samoylov Island – located on a Holocene river terrace within the delta's youngest geomorphological unit – satellite-derived measurements do not indicate distinct long-term subsidence. Instead, they scatter between -0.1 and +0.7 cm/year, i.e. mostly indicating slight apparent uplift. Four of the seven in-situ measurements, on the other hand, show a pronounced downward movement exceeding -2.0 cm/year, while the remaining three sites exhibit smaller rates of motion between -0.5 and -1.4 cm/year. The measurement set up of surface subsidence on Samoylov Island is challenging due to the narrow network of polygonal tundra with highly heterogeneous soil moisture conditions. As shown in Figure 6, in-situ points located in the wetter polygonal centers and on the drier polygonal rims, that have the same satellite-derived deformation values, can differ in subsidence rate by up to 3.8 cm/year. This indicates that, depending on microtopography, soil moisture heterogeneity, and vegetation cover, in-situ displacement measurements can vary on a sub-meter scale—within a range of several centimeters—i.e., at scales finer than the SAR resolution (Antonova et al., 2018). This contrast cannot be attributed to differences in active-layer thickness, since thaw depths in wet polygon centres and dry rims are very similar by the end of the thaw season (Boike et al., 2013). It more likely reflects differences in excess-ice content and in the degradation of the underlying ice wedges. At the satellite's spatial resolution strong sub-metre variability in displacement is not resolved, and a single in-situ point is not necessarily representative of the corresponding resolution cell (Michaelides et al., 2019). In addition, two factors related to the DInSAR processing chain may further affect the accuracy of the derived motion (Strozzi et al., 2018). First, undersampling of SAR data in local areas experiencing large movement rates can lead to phase unwrapping errors and an underestimation of the motion. Second, the noise filter applied in our DInSAR processing chain may also introduce an underestimation of the subsidence. Nevertheless, it cannot be excluded that the temporal discrepancies between satellite acquisitions and ground measurements also account for a portion of the observed differences.

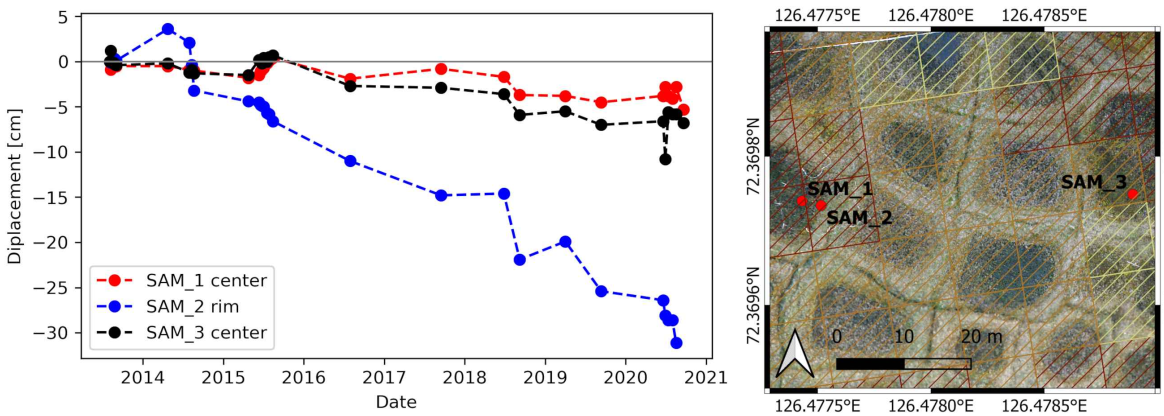

(a) (b)

Figure 6: (a) Displacement time series for three in-situ measurement points on Samoylov Island, located at the center and along the rim of polygonal tundra features. (b) Map showing the locations of the in-situ points plotted in (a), background map by Boike et al. (2015), overlain with the DInSAR raster grid (hashed). Hash colors indicating the DInSAR-derived displacement rate correspond to the color bar shown in Figure 3.

Both in-situ and satellite measurements on Kurungnakh-Sise Island, which belongs to the Yedoma geomorphological unit, reveal a pronounced downward movement of a few centimeters per year (in-situ mean -2.4 cm/year, satellite mean -1.9 cm/year). However, in-situ values exhibit greater variability than satellite-derived measurements (in-situ standard deviation 1.2 cm/year, satellite standard deviation 0.7 cm/year). Within a single satellite pixel, in-situ measurements can span a wide range of long-term displacement rates, with differences of up to 2.9 cm/year. The lowest in-situ subsidence rates within a pixel are closest to the satellite-derived values, whereas higher in-situ deformation rates generally correspond to pixels with larger satellite-derived rates. Compared to Samoylov Island, field measurements on Kurungnakh-Sise Island are more representative at the satellite scale. This is attributed to larger continuous surfaces and more homogeneous soil moisture conditions, which together result in more uniform terrain. At some measurement sites, however, local thermo-erosional processes occur, resulting in large subsidence rates of up to 5 cm/year. Consequently, the field points can capture local extremes, whereas satellite resolution is not representative of such specific local conditions. In these cases, the satellite may smooth local variability rather than underestimate it.

https://doi.org/10.5194/egusphere-2026-5477
Preprint. Discussion started: 22 September 2026

5 Discussion

5.1 Sentinel-1 quality assessment and calibration

In mid-latitude urban environments, the primary sources of error in DInSAR quality are tropospheric delays and phase noise. For C-band measurements over urban areas, where coherence remains consistently high over multi-year intervals comparable to that observed over lowland permafrost sites within 12-days repeat passes, Crosetto et al. (2009) estimated an error of 6–7 mm per interferogram, partitioned into noise-related (approximately 1–2 mm) and atmospheric (approximately 5–6 mm) contributions. Owing to the lower coherence between late-summer acquisitions from consecutive years (values of approximately 0.2; Supplementary Figure B1), we adopt in the present study a per-interferogram error of 7 mm. To derive displacement rates, we considered 58 interferograms (Supplementary Table B1), representing a cumulative temporal baseline of 15.4 years. Applying the stacking error propagation framework of Strozzi et al. (2001), we obtain a displacement-rate precision of 3.4 mm/year. We interpret this value as the intrinsic precision of our results and highlight that the observed velocity differences across the three geomorphological units of the Lena Delta are larger than this value.

Several regions in the long-term displacement rate map (Figure 3) exhibit slight positive values, notably on the Pleistocene sandy geomorphological unit dominated by a dry land surface, an observation also reflected in the histogram presented in Figure 7. The Samoylov research station located on the Holocene terrace, constructed in 2015 and which could have been potentially used as stable target because of the foundations driven deep into the stable, permanently frozen ground, also shows a heave rate of 0.5 cm/year. Similarly, apparent uplift signals are observed in floodplain areas in Figure 4, such as on the northwest side of Samoylov Island. Rather than interpreting these positive displacement rates as genuine uplift (e.g., due to tectonic activity or ice aggregation), we currently attribute them to calibration inaccuracies and atmospheric compensation artifacts. Future analyses incorporating longer temporal satellite image series or alternative atmospheric compensation strategies may help reduce this limitation.

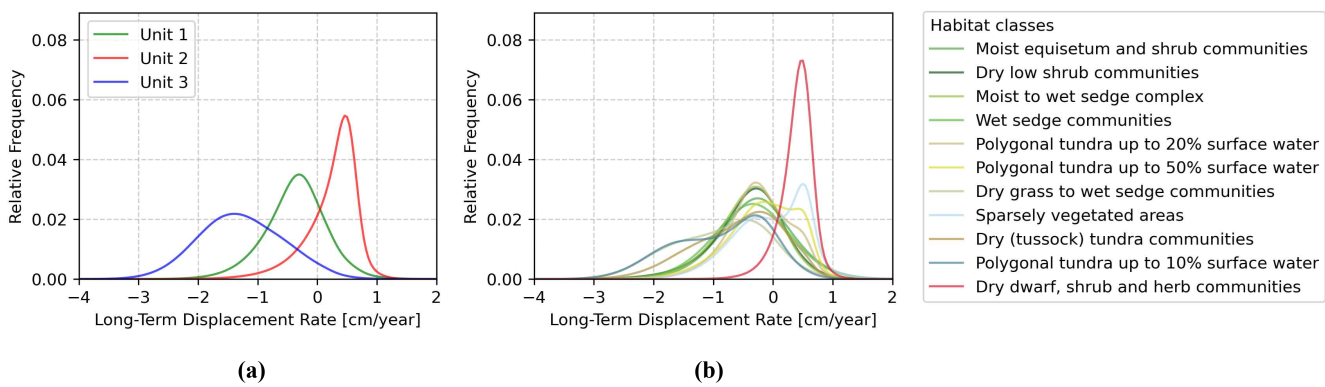

Figure 7: Histograms showing the long-term displacement rate for (a) the three geomorphological units of the Lena Delta and (b) the habitat classes (Lisovski et al., 2023). Unit 1 is the youngest geomorphological unit with river Holocene terraces and modern floodplains, Unit 2 is the Pleistocene sand-dominated geomorphological unit, and Unit 3 is the Yedoma geomorphological unit.

https://doi.org/10.5194/egusphere-2026-5477
Preprint. Discussion started: 22 September 2026

For low-land permafrost we should also take into account possible effects on the DInSAR phase of varying soil moisture and vegetation conditions (De Zan and Gomba, 2018). The presence and systematic bias of these variables in differential interferometry limits the accuracy of the estimated deformation. The extent to which water level and soil moisture fluctuations and vegetation growth – occurring concurrently with subsidence – affect the DInSAR analysis is not specifically addressed in this study. But, as argued in Strozzi et al. (2026) using coincident satellite SAR at different bands (L-, C- and X-), surface displacement remains the dominant contributor to the DInSAR phase relative to soil moisture variations, whose influence increases with wavelength due to greater penetration depth at lower frequencies, and vegetation effects, which tend to introduce stronger systematic distortions at higher frequencies. In the same study (Strozzi et al., 2026), vegetation leaf-out was determined from time-lapse camera data in 2018. As it began in late May, it occurred prior to the DInSAR analyses.
Finally, we recall from Section 4.2 that strong variations in displacement at the sub-meter scale are biased at the satellite's spatial resolution. Furthermore, a noise filter was applied in our DInSAR processing chain and undersampling of SAR data in local areas experiencing large movement rates can lead to phase unwrapping errors. As observed in Figure 5, these three effects lead to an underestimation of the satellite-derived displacement compared to in-situ data.
Taken together, the considerations discussed throughout this section suggest that satellite-derived velocity differences of a few mm/year between neighboring regions within the delta are physically meaningful, although underestimated relative to in-situ measurements. We reiterate, however, that the spatial patterns of vertical displacement should be interpreted primarily in relative terms, rather than as absolute values, as the subsidence rates may be slightly underestimated.

5.2 Permafrost degradation

The most remarkable outcome of our DInSAR measurements is the clear spatial correspondence between long-term vertical displacement rates (Figure 3) and independently mapped habitat classes (Figure 1), land cover units and ground types (Figure 1 and Appendix A). The subsurface stratigraphy of the three geomorphological units of the Lena Delta results in markedly different soil thermal regimes and varying susceptibility to soil surface warming, as suggested by a modelling study by Westermann et al. (2017). The histogram of the long-term displacement rates over the three geomorphological units (Figure 7a) illustrate indeed a clear distinction of the rates of motion between the Yedoma unit and the Pleistocene sand-dominated unit, with intermediate values over the youngest geomorphological unit.
The Yedoma geomorphological unit, where a clear subsidence signal is depicted by the long-term displacement rate (Figures 3 and 7a), is richest in ground ice, making it highly susceptible to fast degradation processes. The high ice content of this geomorphological unit is also confirmed by the map of ground ice content of Shestakova et al. (2021) (Appendix A1a), indicating a predominant ice content class of 60-80 % (Appendix A2a) and the highest long-term displacement rate for this class (Appendix A3a). Degradation is often extensive, especially subsidence due to drainage at the break-off edges. In terms of cryogenic processes (Shestakova et al., 2021) (Appendix A1b), thermokarst processes prevail here as the dominant cryogenic processes (Appendix A2b). This class also exhibits the highest long-term subsidence values (Appendix A3b). Patches of frost cracking and frost heave areas can also be found within this geomorphological unit. However, this class

https://doi.org/10.5194/egusphere-2026-5477
Preprint. Discussion started: 22 September 2026

shows a bimodal distribution in the histogram of Appendix A3b, which can be attributed to the fact that it is not exclusively confined to the Yedoma unit but also occurs in the northern parts of the youngest geomorphological unit. The two habitat classes exhibiting the most pronounced subsidence values – polygonal tundra and dry grass to wet sedge communities (Figures 7b) – are predominantly associated with the Yedoma unit (Figures 2). However, no pronounced differentiation is observed among habitat classes with significantly larger subsidence. In contrast, the circumarctic land cover units (Appendix A1c) do reveal a clear distinction between classes with markedly higher subsidence. The two land cover units characterized by the most substantial subsidence values are moist tundra with abundant moss and low shrubs (Appendix A3c), which occur most frequently on the Yedoma unit (Appendix A2c).

The second geomorphological unit is sandy, of Pleistocene origin and described as ice-poor compared to the other two units (Westermann et al., 2017). This is consistent with the long-term deformation values observed here, where this geomorphological unit appears to be the most stable (Figures 3 and 7a). Among the most common habitat classes are dry dwarf, shrub and herb communities (Figure 2), which are very dry with low biomass and show the lowest subsidence values (Figure 7b). Only in the thermokarst basins there are wetter and ice-rich younger Holocene deposits containing numerous patches of decomposable biomass (Figure 1). However, such a spatial difference is not apparent in the long-term displacement rate map (Figure 3). The ice content map of Shestakova et al. (2021) fits less well with the observed deformation patterns. In this map (Appendix A1a), patches of ice content classes of 40-60 %, found on both the sandy Pleistocene and Yedoma units, appear to be more stable than areas classified as having lower ice content of 20-40 % (Appendix A3a), which occur on the sandy Pleistocene unit and predominantly on the youngest parts. However, it is not clear whether the ice-rich layers are situated directly below the active layer or at deeper depths. In the latter case, warming would likely result in active layer deepening rather than ice melt and ground subsidence, which would be in line with the DInSAR observations. The cryogenic process class ’frost cracking’, on the other hand, which dominates the sandy Pleistocene unit (Appendix A1b), exhibits values that are the most stable of all classes (Appendix A1c). This relationship is even stronger with the land cover class ‘dry to moist tundra, partially barren, prostrate shrubs’ (Appendix A3c), which dominates the sandy Pleistocene unit (Appendix A2c).

In the youngest geomorphological unit, the subsidence values are moderate, lying between the higher values observed on the Yedoma unit and the more stable values of the sandy Pleistocene unit (Figure 3 and 7a). Polygonal tundra up to 20 % surface water is the dominant habitat class (Figure 2), while wet and wetland land cover units, both on the Holocene terraces and in the wetland parts of the active floodplains, are the dominant land cover units (Appendix A2c). The Holocene polygonal ice wedge network on the Holocene terraces is much smaller than that of Pleistocene origin found on the Yedoma unit. In addition, there are many more ponds, which indicate that it is also rich in ground ice and exhibits higher ice content than suggested by the map of Shestakova et al. (2021) (Appendix A1a). Degradation here is rather local, but also extensive near the eroding margins of the islands.

https://doi.org/10.5194/egusphere-2026-5477
Preprint. Discussion started: 22 September 2026

6 Conclusions

Long-term subsidence in permafrost regions is generally attributed to permafrost degradation and the melting of ground ice at the top of the permafrost layer (Zwieback et al., 2024), representing a direct impact of changing climatic conditions. In the Lena Delta, our DInSAR results demonstrate that long-term deformation rates vary significantly among the three geomorphological units and are closely linked to the measured and inferred ground ice content (Westermann et al., 2017). The strongest subsidence occurs on the Yedoma unit, characterized by abundant ground ice and dominated by thermokarst processes (Shestakova et al., 2021). The observed high deformation rates are therefore indicative of ongoing ground ice melting in this ice-rich unit. In contrast, the sandy Pleistocene unit is the most stable, showing the lowest displacement rates. This stability coincides with low ground ice content and dry vegetation cover.

Monitoring thaw subsidence is critically important in the context of rapid Arctic warming (e.g., Rowland et al., 2010; Forster et al., 2023). Even if small by magnitude, when integrated over extensive regions, isotropic thaw subsidence may be responsible for thawing large volumes of carbon-rich substrate, eventually leading to the release of substantial amounts of CO_2 and CH_4 into the atmosphere and hydrosphere. Subsidence may have widespread negative impacts on existing infrastructure (Shiklomanov et al., 2013). Therefore, the development of systematic monitoring of thaw subsidence is urgently needed to deliver consistent and continuous exchange of data across different permafrost regions (Streletskiy et al., 2025). To address these challenges, the integration of coordinated field observations, remote sensing, and modeling of thaw subsidence across a range of spatial and temporal scales is required. The Lena Delta is a high-latitude site where the effects of Arctic warming and their consequences for the landscape are only beginning to emerge. The in-situ subsidence monitoring sites in the Lena Delta that took place in the last decade provide the only ground-based data for this area—and no additional ground-based data are expected to be available for this area in the near future. Remote sensing offers a valuable tool for capturing this large-scale landscape response, complementing and extending localized field measurements in time and space.

We have shown that monitoring long-term ground surface subsidence is feasible over the Lena River region using Sentinel-1 satellite data. However, this approach requires several prerequisites. First, a long series of SAR images for continuous monitoring is essential. Unfortunately, no additional IW swath mode images have been acquired over northern Siberia since the failure of Sentinel-1B in 2021 and acquisitions only resumed with the commissioning of Sentinel-1C in 2025. This data gap currently limits the temporal coverage of our analyses and our Sentinel-1 displacement time series are not yet long enough or sufficiently consistent across years to conclusively capture the effects of warmer years after 2018. Second, long-term coherence between acquisitions is required. While this condition is generally met in the study area, it cannot always be guaranteed across all surface types and seasons in order to extend a similar analysis to other Arctic areas (Bartsch et al., 2026). For this purpose, longer-wavelength SAR systems (e.g., L-band) can achieve better performance than C-band, particularly in vegetated or rapidly deforming areas, due to reduced sensitivity to temporal decorrelation and greater phase ambiguity intervals. Third, an effective strategy for atmospheric phase screen reduction is still needed (Gomba et al., 2016;

https://doi.org/10.5194/egusphere-2026-5477
Preprint. Discussion started: 22 September 2026

Wegmüller et al., 2024). The unavailability of the Extended Timing Annotation Dataset (ETAD) for Sentinel-1 (Gisinger et al., 2022) before July 2023, for instance, did not allow us to exploit it in our work.

Summer thaw displacement, which is primarily sensitive to ground ice melt within the active layer (Wendt et al., 2026), was the subject of an earlier study about the Lena Delta (Strozzi et al., 2026). Working specifically on Samoylov Island, the study measured summer thaw displacement of several centimeters in the wet areas of the island's western floodplain and lower and more heterogeneous values over the Holocene river terrace in the central and eastern part of the island. These findings illustrated that the large-scale magnitude of seasonal deformation is predominantly related to soil type and moisture conditions. Analyzing the relationship between summer thaw displacement, long-term subsidence, land cover classes, ground ice content, active layer thickness, and possibly also the Normalized Difference Moisture Index (NDMI) (Gao, 1996) at the scale of the Lena Delta warrants further detailed investigations.

Data availability

The Sentinel-1 imagery used in this study is available from Copernicus. The TanDEM-X data is available from DLR under licence and cannot be redistributed by the authors. The habitat classes, ground ice content, cryogenic processes and circumarctic land cover units are available from the original data providers cited in the manuscript.

Acknowledgements

Sentinel-1 images available from Copernicus. TanDEM-X data are courtesy of DEM_GEOL1365, copyright DLR.

Author contributions

Tazio Strozzi: Writing – original draft, Visualization, Methodology, Formal analysis, Data curation, Conceptualization. Barbara Widhalm: Writing – original draft, Visualization, Formal analysis. Nina Jones: Writing – original draft, Data curation. Julia Boike: Writing – review & editing, Validation, Investigation. Sofia Antonova: Writing – review & editing, Validation. Birgit Heim: Writing – review & editing. Sebastian Westermann: Writing – review & editing, Supervision, Conceptualization. Andreas Kääb: Writing – review & editing, Supervision, Conceptualization. Annett Bartsch: Writing – review & editing, Funding acquisition.

Competing interests

At least one of the (co-)authors is a member of the editorial board of Earth Observation.

https://doi.org/10.5194/egusphere-2026-5477
Preprint. Discussion started: 22 September 2026

Appendix A: Ground ice content, cryogenic processes and circumarctic land cover units

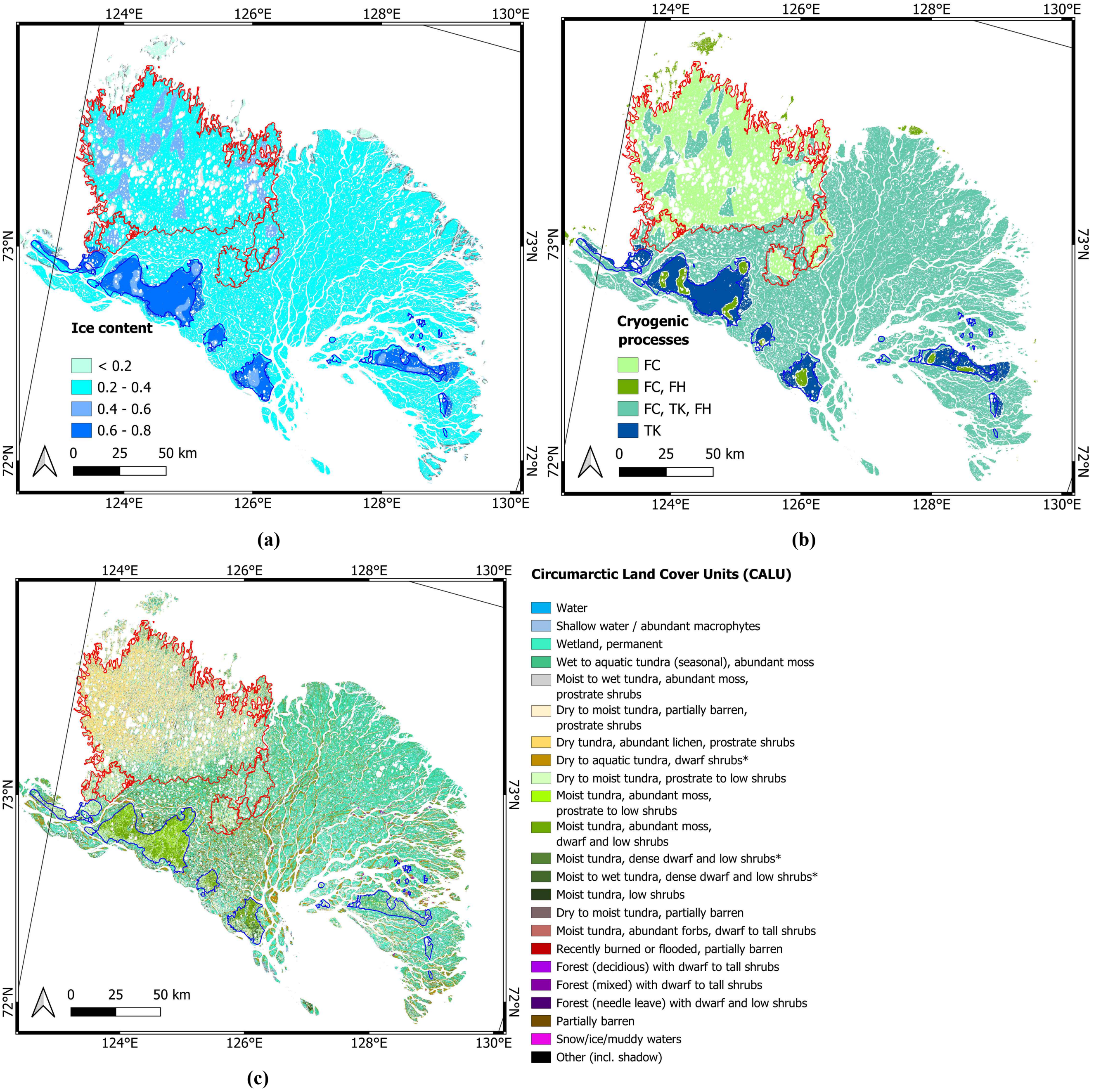

Figure A1. Maps of (a) volumetric ground ice content of surface sediments in fraction (Shestakova et al., 2021), (b) cryogenic processes (Shestakova et al., 2021) (FC - frost cracking, FH - frost heaving, TK – thermokarst) and (c) circumarctic land cover units (Bartsch et al., 2024) of the Lena Delta. The extension of the sand dominated geomorphological unit is shown in red and that of the Yedoma geomorphological unit in blue; the remaining areas are the youngest geomorphological unit, with Holocene river terraces and modern floodplains. The footprint of the Sentinel-1 images is shown with a dashed black line. Masking was applied according to Figure 1, excluding the habitat classes water and sand.

https://doi.org/10.5194/egusphere-2026-5477
Preprint. Discussion started: 22 September 2026

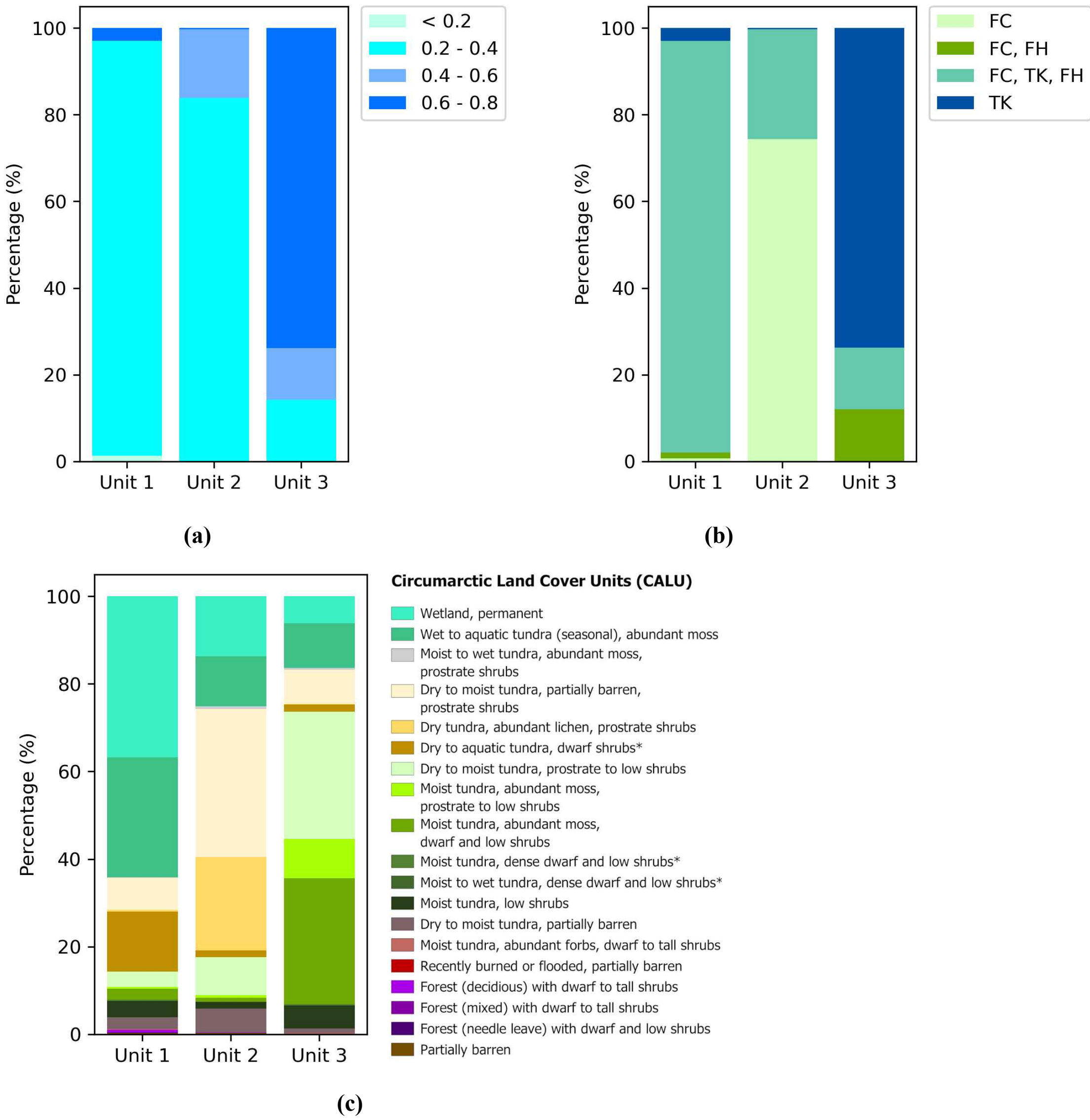

Figure A2. Bar plot showing the proportion of classes within the three geomorphological units of the Lena Delta. (a) Ice content classes (Shestakova et al., 2021), (b) cryogenic processes (Shestakova et al., 2021): FC - frost cracking, FH - frost heaving, TK – thermokarst, and (c) circumarctic land cover units (Bartsch et al., 2024). Unit 1 is the youngest geomorphological unit with Holocene terraces and modern floodplains, Unit 2 is the Pleistocene sand-dominated geomorphological unit, and Unit 3 is the Yedoma geomorphological unit.

https://doi.org/10.5194/egusphere-2026-5477
Preprint. Discussion started: 22 September 2026

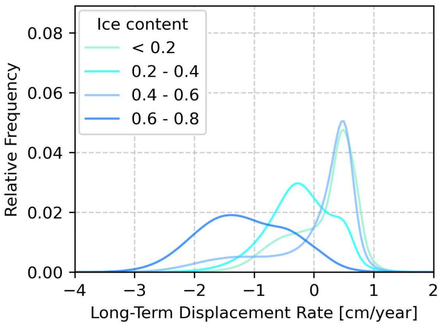

(a)

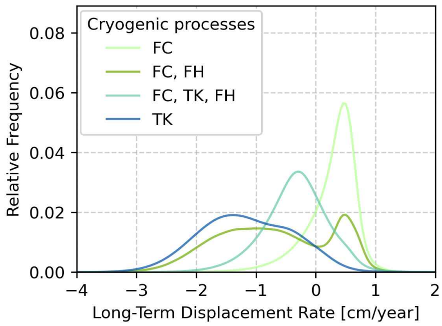

(b)

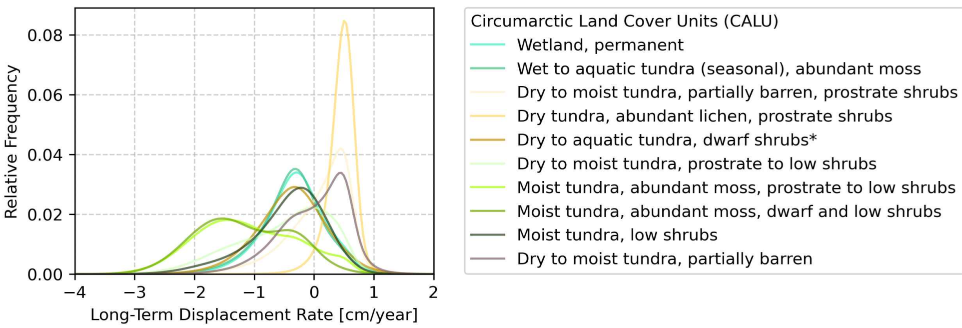

(c)

Figure A3. Histograms showing the long-term displacement rate for (a) the ice content classes (Shestakova et al., 2021) (values given in fractions), (b) the cryogenic processes (Shestakova et al., 2021) (FC - frost cracking. FH - frost heaving. TK – thermokarst) and (c) the predominant circumarctic land cover units (Bartsch et al., 2024).

https://doi.org/10.5194/egusphere-2026-5477
Preprint. Discussion started: 22 September 2026

Appendix B: Satellite SAR data

Table B1. List of Sentinel-1 SAR data. Reference SLC is 20180730, all other images are co-registered to the reference.

Date 1	Date 2	Temp. baseline (days)	Perp. baseline (m)
20160722	20160803	12	34.2
20160803	20160815	12	-49.2
20160815	20160827	12	-76.8
20160827	20160908	12	-8.1
20160908	20160926	18	98.9
20170629	20170711	12	96.4
20170711	20170723	12	7.6
20170723	20170804	12	14.1
20170804	20170816	12	-146.0
20170816	20170828	12	48.0
20170828	20170909	12	66.7
20170909	20170921	12	44.2
20170921	20171003	12	-26.9
20180612	20180624	12	-42.4
20180624	20180706	12	-68.2
20180706	20180718	12	-50.1
20180718	20180730	12	69.5
20180730	20180811	12	92.5
20180811	20180823	12	-72.5
20180823	20180904	12	-30.4
20180904	20180916	12	-11.4
20180916	20180928	12	51.0
20180928	20181010	12	76.5
20190619	20190701	12	34.8
20190701	20190713	12	-58.3
20190713	20190725	12	-108.2
20200613	20200625	12	-16.3
20200625	20200707	12	59.7
20200707	20200719	12	21.7
20200719	20200731	12	14.8
20200731	20200812	12	-135.5
20200812	20200824	12	16.1
20200824	20200905	12	95.2
20200905	20200917	12	57.1
20200917	20200929	12	-69.0
20200929	20201011	12	-78.1
20210527	20210608	12	0.4
20210608	20210620	12	-47.7
20210620	20210702	12	-49.0
20210702	20210714	12	5.4
20210714	20210726	12	7.1
20210726	20210831	36	-52.3
20210831	20210912	12	30.4
20210912	20210924	12	83.8
20160803	20170804	366	-12.6
20160815	20170828	378	-61.5
20160827	20170828	366	15.3
20160827	20170909	378	82.0
20160908	20170921	378	134.3
20170909	20180904	360	-61.8
20170909	20180916	372	-73.2
20170921	20180928	372	-66.4
20180904	20190725	324	-36.3
20180916	20190725	312	-24.9
20190725	20200719	360	122.3
20200824	20210831	372	-25.1
20200905	20210912	372	-89.9
20200917	20210924	372	-63.2

https://doi.org/10.5194/egusphere-2026-5477
Preprint. Discussion started: 22 September 2026

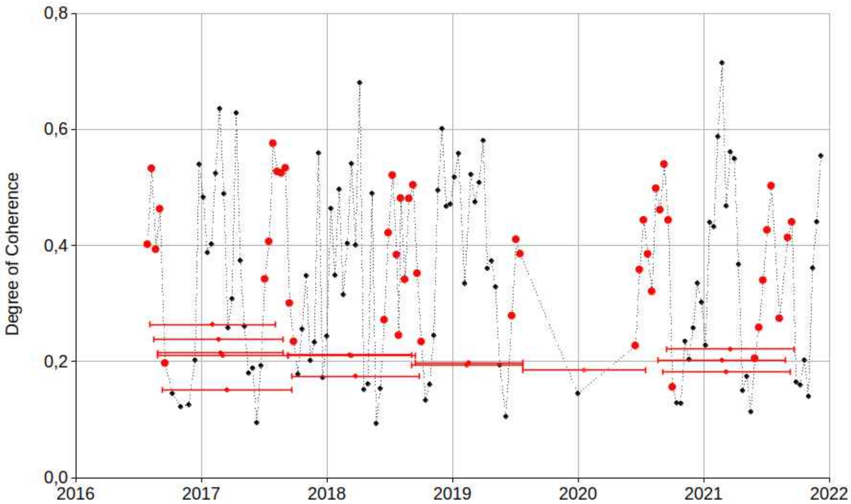

510 **Figure B1. Degree of coherence (in short coherence) of Sentinel-1 interferograms over the Lena Delta. Our processing sequence is based on the sequential 12- to 36-days summer interferograms of each year from 2016 to 2021 and the few differential interferograms of 1-year temporal baselines, shown in red and listed in Supplementary Table B1. The coherence is very low (values close to 0.1) during snowmelt in early summer and for the first snow fall in late summer, which precludes the possibility of successful phase unwrapping. During the snow-free period from June to September of each year, the coherence is usually above**
515 **0.3. Additionally, there is enough coherence (values of about 0.2) between late summer data of consecutive years. The coherence is also usually above 0.3 during periods of stable cold weather in winter, but winter data of consecutive years cannot be connected due to the very low coherence (values of about 0.1, not shown in the graph).**

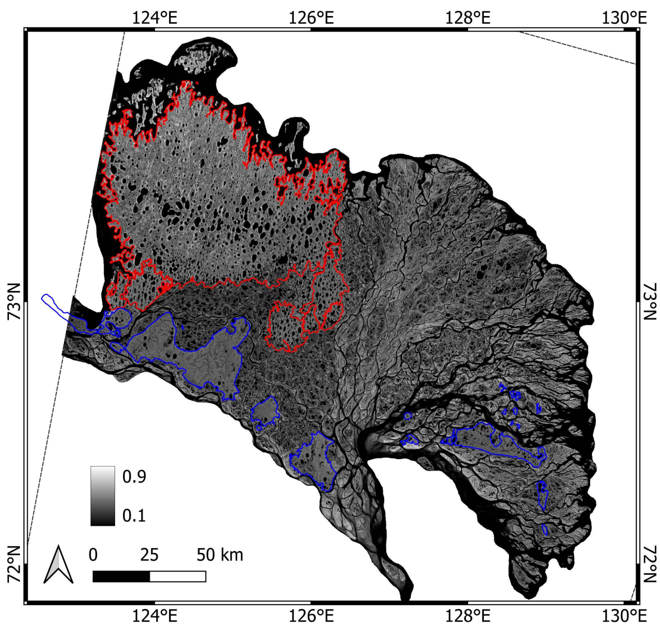

Figure B2. Mean 12-days coherence map of the Lena Delta. The extent of the sand-dominated geomorphological unit is shown by
520 **red outlines and that of the Yedoma geomorphological unit by blue outlines; the remaining areas are the youngest geomorphological unit, with Holocene terraces and the modern floodplains. The footprint of the Sentinel-1 images is shown with a dashed black line.**

Disclaimer

Publisher's note: Copernicus Publications remains neutral with regard to jurisdictional claims made in the text, published maps, institutional affiliations, or any other geographical representation in this paper. The authors bear the ultimate responsibility for providing appropriate place names. Views expressed in the text are those of the authors and do not necessarily reflect the views of the publisher.

Financial support

This research has been supported by the European Space Agency CCI Permafrost Project (grant no. 4000123681/18/I-NB). AK acknowledges additional support by ESA EarthExplorer 10 Harmony studies (grant no. 4000135083/21/NL/FF/ab).

Review statement

The review statement will be added by Copernicus Publications listing the handling editor as well as all contributing referees according to their status anonymous or identified.

References

Aga, J., Boike, J., Langer, M., Ingeman-Nielsen, T., and Westermann, S.: Simulating ice segregation and thaw consolidation in permafrost environments with the CryoGrid community model, The Cryosphere, 17, 4179–4206, https://doi.org/10.5194/tc-17-4179-2023, 2023.

Antonova, S., Sudhaus, H., Strozzi, T., Zwieback, S., Kääb, A., Heim, B., Langer, M., Bornemann, N., and Boike, J.: Thaw Subsidence of a Yedoma Landscape in Northern Siberia, Measured In Situ and Estimated from TerraSAR-X Interferometry, Remote Sensing, 10, 494, https://doi.org/10.3390/rs10040494, 2018.

Are, F. and Reimnitz, E.: An Overview of the Lena River Delta Setting: Geology, Tectonics, Geomorphology, and Hydrology, Journal of Coastal Research, 16, 4, 1083–1093, https://www.jstor.org/stable/4300125, 2000.

Bamler, R. and Hartl, P.: Synthetic aperture radar interferometry, Inverse Problems, 14, R1–R54, https://doi.org/10.1088/0266-5611/14/4/001, 1998.

Bartsch, A., Efimova, A., Widhalm, B., Muri, X., von Baeckmann, C., Bergstedt, H., Ermokhina, K., Hugelius, G., Heim, B., and Leibman, M.: Circumarctic land cover diversity considering wetness gradients, Hydrol. Earth Syst. Sci., 28, 2421–2481, https://doi.org/10.5194/hess-28-2421-2024, 2024.

Bartsch, A., Widhalm, B., Radha Krishnan, S. R., and Liu, Z.: Tracking land surface deformation in lowland permafrost regions across the Arctic exploiting the first decade of Copernicus Sentinel-1, Remote Sensing of Environment, 340, 115409, https://doi.org/10.1016/j.rse.2026.115409, 2026.

Berardino, P., Fornaro, G., Lanari, R., and Sansosti, E.: A new algorithm for surface deformation monitoring based on small baseline differential SAR interferograms, IEEE Trans. Geosci. Remote Sensing, 40, 2375–2383, https://doi.org/10.1109/tgrs.2002.803792, 2002.

Boike, J., Kattenstroth, B., Abramova, K., Bornemann, N., Chetverova, A., Fedorova, I., Fröb, K., Grigoriev, M., Grüber, M., Kutzbach, L., Langer, M., Minke, M., Muster, S., Piel, K., Pfeiffer, E.-M., Stoof, G., Westermann, S., Wischnewski, K., Wille, C., and Hubberten, H.-W.: Baseline characteristics of climate, permafrost and land cover from a new permafrost observatory in the Lena River Delta, Siberia (1998–2011), Biogeosciences, 10, 2105–2128, https://doi.org/10.5194/bg-10-2105-2013, 2013.

Boike, J., Veh, G., Viitanen, L.-K., Bornemann, N., Stoof, G., and Muster, S.: Visible and near-infrared orthomosaic of Samoylov Island, Siberia, summer 2015 (5.3 GB), https://doi.org/10.1594/PANGAEA.845724, 2015.

Boike, J., Nitzbon, J., Anders, K., Grigoriev, M., Bolshiyanov, D., Langer, M., Lange, S., Bornemann, N., Morgenstern, A., Schreiber, P., Wille, C., Chadburn, S., Gouttevin, I., Burke, E., and Kutzbach, L.: A 16-year record (2002–2017) of permafrost, active-layer, and meteorological conditions at the Samoylov Island Arctic permafrost research site, Lena River delta, northern Siberia: an opportunity to validate remote-sensing data and land surface, snow, and permafrost models, Earth Syst. Sci. Data, 11, 261–299, https://doi.org/10.5194/essd-11-261-2019, 2019.

Costantini, M.: A novel phase unwrapping method based on network programming, IEEE Trans. Geosci. Remote Sensing, 36, 813–821, https://doi.org/10.1109/36.673674, 1998.

Crosetto, M., Monserrat, O., Bremmer, C., Hanssen, R., Capes, R., and Marsh, S.: Ground motion monitoring using SAR interferometry: Quality assessment, European Geologist Magazine, 26, 12–15, 2009.

De Zan, F. and Gomba, G.: Vegetation and soil moisture inversion from SAR closure phases: First experiments and results, Remote Sensing of Environment, 217, 562–572, https://doi.org/10.1016/j.rse.2018.08.034, 2018.

Farzamian, M., Vieira, G., Monteiro Santos, F. A., Yaghoobi Tabar, B., Hauck, C., Paz, M. C., Bernardo, I., Ramos, M., and de Pablo, M. A.: Detailed detection of active layer freeze–thaw dynamics using quasi-continuous electrical resistivity tomography (Deception Island, Antarctica), The Cryosphere, 14, 1105–1120, https://doi.org/10.5194/tc-14-1105-2020, 2020.

Forbes, D. L., Craymer, M. R., James, T. S., and Whalen, D.: Subsidence drives habitat loss in a large permafrost delta, Mackenzie River outlet to the Beaufort Sea, western Arctic Canada, Can. J. Earth Sci., 59, 914–934, https://doi.org/10.1139/cjes-2021-0127, 2022.

Forster, P. M., Smith, C. J., Walsh, T., Lamb, W. F., Lamboll, R., Hauser, M., Ribes, A., Rosen, D., Gillett, N., Palmer, M. D., Rogelj, J., von Schuckmann, K., Seneviratne, S. I., Trewin, B., Zhang, X., Allen, M., Andrew, R., Birt, A., Borger, A., Boyer, T., Broersma, J. A., Cheng, L., Dentener, F., Friedlingstein, P., Gutiérrez, J. M., Gütschow, J., Hall, B., Ishii, M., Jenkins, S., Lan, X., Lee, J.-Y., Morice, C., Kadow, C., Kennedy, J., Killick, R., Minx, J. C., Naik, V., Peters, G. P., Pirani, A., Pongratz, J., Schleussner, C.-F., Szopa, S., Thorne, P., Rohde, R., Rojas Corradi, M., Schumacher, D., Vose, R., Zickfeld, K., Masson-Delmotte, V., and Zhai, P.: Indicators of Global Climate Change 2022: annual update of large-scale

https://doi.org/10.5194/egusphere-2026-5477
Preprint. Discussion started: 22 September 2026

indicators of the state of the climate system and human influence, Earth Syst. Sci. Data, 15, 2295–2327, https://doi.org/10.5194/essd-15-2295-2023, 2023.

Gao, B.: NDWI—A normalized difference water index for remote sensing of vegetation liquid water from space, Remote Sensing of Environment, 58, 257–266, https://doi.org/10.1016/s0034-4257(96)00067-3, 1996.

Gisinger, C., Libert, L., Marinkovic, P., Krieger, L., Larsen, Y., Valentino, A., Breit, H., Balss, U., Suchandt, S., Nagler, T., Eineder, M., and Miranda, N.: The Extended Timing Annotation Dataset for Sentinel-1—Product Description and First Evaluation Results, IEEE Trans. Geosci. Remote Sensing, 60, 1–22, https://doi.org/10.1109/tgrs.2022.3194216, 2022.

Goldstein, R. M. and Werner, C. L.: Radar interferogram filtering for geophysical applications, Geophysical Research Letters, 25, 4035–4038, https://doi.org/10.1029/1998gl900033, 1998.

Gomba, G., Parizzi, A., De Zan, F., Eineder, M., and Bamler, R.: Toward Operational Compensation of Ionospheric Effects in SAR Interferograms: The Split-Spectrum Method, IEEE Trans. Geosci. Remote Sensing, 54, 1446–1461, https://doi.org/10.1109/tgrs.2015.2481079, 2016.

Grigoriev, M. N.: Cryomorphogenesis of the Lena River mouth area. Yakutsk: Permafrost Institute Press, p.176. (in Russian), 1993.

Grosse, G., Romanovsky, V., Jorgenson, T., Anthony, K. W., Brown, J., and Overduin, P. P.: Vulnerability and Feedbacks of Permafrost to Climate Change, EoS Transactions, 92, 73–74, https://doi.org/10.1029/2011eo090001, 2011.

Hanssen, R. F.: Radar Interferometry, Springer Netherlands, https://doi.org/10.1007/0-306-47633-9, 2001.

Hersbach, H., Bell, B., Berrisford, P., Hirahara, S., Horányi, A., Muñoz-Sabater, J., Nicolas, J., Peubey, C., Radu, R., Schepers, D., Simmons, A., Soci, C., Abdalla, S., Abellan, X., Balsamo, G., Bechtold, P., Biavati, G., Bidlot, J., Bonavita, M., De Chiara, G., Dahlgren, P., Dee, D., Diamantakis, M., Dragani, R., Flemming, J., Forbes, R., Fuentes, M., Geer, A., Haimberger, L., Healy, S., Hogan, R. J., Hólm, E., Janisková, M., Keeley, S., Laloyaux, P., Lopez, P., Lupu, C., Radnoti, G., de Rosnay, P., Rozum, I., Vamborg, F., Villaume, S., and Thépaut, J.: The ERA5 global reanalysis, Quart J Royal Meteoro Soc, 146, 1999–2049, https://doi.org/10.1002/qj.3803, 2020.

Heim, B., Lisovski, S., Wieczorek, M., Morgenstern, A., Juhls, B., Shevtsova, I., Kruse, S., Boike, J., Fedorova, I., and Herzschuh, U.: Spring snow cover duration and tundra greenness in the Lena Delta, Siberia: two decades of MODIS satellite time series (2001–2021), Environ. Res. Lett., 17, 085005, https://doi.org/10.1088/1748-9326/ac8066, 2022.

Lisovski, S., Runge, A., Shevtsova, I., Landgraf, N., Morgenstern, A., Okoth, R. R., Fuchs, M., Lashchinskiy, N., Stadie, C., Beamish, A., Herzschuh, U., Grosse, G., and Heim, B.: A new habitat map of the Lena Delta in Arctic Siberia based on field and remote sensing datasets, Earth Syst. Sci. Data, 17, 1707–1730, https://doi.org/10.5194/essd-17-1707-2025, 2025.

Michaelides, R. J., Zebker, H. A., and Zheng, Y.: An Algorithm for Estimating and Correcting Decorrelation Phase From InSAR Data Using Closure Phase Triplets, IEEE Trans. Geosci. Remote Sensing, 57, 10390–10397, https://doi.org/10.1109/tgrs.2019.2934362, 2019.

Michaelides, R. J., Chen, R. H., Zhao, Y., Schaefer, K., Parsekian, A. D., Sullivan, T., Moghaddam, M., Zebker, H. A., Liu, L., Xu, X., and Chen, J.: Permafrost Dynamics Observatory—Part I: Postprocessing and Calibration Methods of UAVSAR

L-Band InSAR Data for Seasonal Subsidence Estimation, Earth and Space Science, 8, https://doi.org/10.1029/2020ea001630, 2021.

Morgenstern, A., Grosse, G., Günther, F., Fedorova, I., and Schirrmeister, L.: Spatial analyses of thermokarst lakes and basins in Yedoma landscapes of the Lena Delta, The Cryosphere, 5, 849–867, https://doi.org/10.5194/tc-5-849-2011, 2011.

Morgenstern, A., Ulrich, M., Günther, F., Roessler, S., Fedorova, I. V., Rudaya, N. A., Wetterich, S., Boike, J., and Schirrmeister, L.: Evolution of thermokarst in East Siberian ice-rich permafrost: A case study, Geomorphology, 201, 363–379, https://doi.org/10.1016/j.geomorph.2013.07.011, 2013.

Obu, J., Westermann, S., Bartsch, A., Berdnikov, N., Christiansen, H. H., Dashtseren, A., Delaloye, R., Elberling, B., Etzelmüller, B., Kholodov, A., Khomutov, A., Kääb, A., Leibman, M. O., Lewkowicz, A. G., Panda, S. K., Romanovsky, V., Way, R. G., Westergaard-Nielsen, A., Wu, T., Yamkhin, J., and Zou, D.: Northern Hemisphere permafrost map based on TTOP modelling for 2000–2016 at 1 km2 scale, Earth-Science Reviews, 193, 299–316, https://doi.org/10.1016/j.earscirev.2019.04.023, 2019.

O'Neill, H. B., Smith, S. L., and Duchesne, C.: Long-Term Permafrost Degradation and Thermokarst Subsidence in the Mackenzie Delta Area Indicated by Thaw Tube Measurements, Cold Regions Engineering 2019, 643–651, https://doi.org/10.1061/9780784482599.074, 2019.

Rowland, J. C., Jones, C. E., Altmann, G., Bryan, R., Crosby, B. T., Hinzman, L. D., Kane, D. L., Lawrence, D. M., Mancino, A., Marsh, P., McNamara, J. P., Romanvosky, V. E., Toniolo, H., Travis, B. J., Trochim, E., Wilson, C. J., and Geernaert, G. L.: Arctic Landscapes in Transition: Responses to Thawing Permafrost, EoS Transactions, 91, 229–230, https://doi.org/10.1029/2010eo260001, 2010.

Rosen, P. A., Hensley, S., Joughin, I. R., Li, F. K., Madsen, S. N., Rodriguez, E., and Goldstein, R. M.: Synthetic aperture radar interferometry, Proc. IEEE, 88, 333–382, https://doi.org/10.1109/5.838084, 2000.

Schirrmeister, L., Kunitsky, V., Grosse, G., Wetterich, S., Meyer, H., Schwamborn, G., Babiy, O., Derevyagin, A., and Siegert, C.: Sedimentary characteristics and origin of the Late Pleistocene Ice Complex on north-east Siberian Arctic coastal lowlands and islands – A review, Quaternary International, 241, 3–25, https://doi.org/10.1016/j.quaint.2010.04.004, 2011.

Schwamborn, G., Rachold, V., and Grigoriev, M. N.: Late Quaternary sedimentation history of the Lena Delta, Quaternary International, 89, 119–134, https://doi.org/10.1016/s1040-6182(01)00084-2, 2002.

Shestakova, A. A., Fedorov, A. N., Torgovkin, Y. I., Konstantinov, P. Y., Vasyliev, N. F., Kalinicheva, S. V., Samsonova, V. V., Hiyama, T., Iijima, Y., Park, H., Iwahana, G., and Gorokhov, A. N.: Mapping the Main Characteristics of Permafrost on the Basis of a Permafrost-Landscape Map of Yakutia Using GIS, Land, 10, 462, https://doi.org/10.3390/land10050462, 2021.

Shiklomanov, N. I., Streletskiy, D. A., Little, J. D., and Nelson, F. E.: Isotropic thaw subsidence in undisturbed permafrost landscapes, Geophysical Research Letters, 40, 6356–6361, https://doi.org/10.1002/2013gl058295, 2013.

https://doi.org/10.5194/egusphere-2026-5477
Preprint. Discussion started: 22 September 2026

Strozzi, T., Antonova, S., Günther, F., Mätzler, E., Vieira, G., Wegmüller, U., Westermann, S., and Bartsch, A.: Sentinel-1 SAR Interferometry for Surface Deformation Monitoring in Low-Land Permafrost Areas, Remote Sensing, 10, 1360, https://doi.org/10.3390/rs10091360, 2018.

Strozzi, T., Wegmüller, U., Tosi, L., Bitelli, G., and Spreckels, V.: Land subsidence monitoring with differential SAR interferometry, Photogrammetric Engineering & Remote Sensing, 67(11), 1261–1270, November 2001.

Strozzi, T., Jones, N., Boike, J., Antonova, S., Heim, B., Leinss, S., Wegmüller, U., Westermann, S., Kääb, A., Grosse, G., and Bartsch, A.: Seasonal vertical surface thaw displacement in 2018 on Samoylov Island (Lena Delta, northeastern Siberia) measured by satellite SAR interferometry with X-, C- and L-band sensors, Remote Sensing of Environment, 335, 115293, https://doi.org/10.1016/j.rse.2026.115293, 2026.

Torres, R., Snoeij, P., Geudtner, D., Bibby, D., Davidson, M., Attema, E., Potin, P., Rommen, B., Floury, N., Brown, M., Traver, I. N., Deghaye, P., Duesmann, B., Rosich, B., Miranda, N., Bruno, C., L'Abbate, M., Croci, R., Pietropaolo, A., Huchler, M., and Rostan, F.: GMES Sentinel-1 mission, Remote Sensing of Environment, 120, 9–24, https://doi.org/10.1016/j.rse.2011.05.028, 2012.

Walker, H.J.: Arctic deltas, Journal of Coastal Research, 14(3):718–738, 1998. ISSN 0749-0208.

Wegmüller, U., Werner, C., Frey, O., and Magnard, C.: Estimation and Compensation of the Ionospheric Path Delay Phase in PALSAR-3 and NISAR-L Interferograms, Atmosphere, 15, 632, https://doi.org/10.3390/atmos15060632, 2024.

Wendt, L., Rouyet, L., Christiansen, H. H., Lauknes, T. R., and Westermann, S.: InSAR sensitivity to active layer ground ice content in Adventdalen, Svalbard, The Cryosphere, 20, 1179–1197, https://doi.org/10.5194/tc-20-1179-2026, 2026.

Werner, C., Strozzi, T., and Wegmuller, U.: Deformation time-series of the lost-hills oil field using a multi-baseline interferometric SAR inversion algorithm with finite difference smoothing constraints, In Proceedings of AGU Fall Meeting, San Francisco, CA, USA, 3–7 December 2012.

Wessel, B., Huber, M., Wohlfart, C., Marschalk, U., Kosmann, D., and Roth, A.: Accuracy assessment of the global TanDEM-X Digital Elevation Model with GPS data, ISPRS Journal of Photogrammetry and Remote Sensing, 139, 171–182, https://doi.org/10.1016/j.isprsjprs.2018.02.017, 2018.

Westermann, S., Peter, M., Langer, M., Schwamborn, G., Schirrmeister, L., Etzelmüller, B., and Boike, J.: Transient modeling of the ground thermal conditions using satellite data in the Lena River delta, Siberia, The Cryosphere, 11, 1441–1463, https://doi.org/10.5194/tc-11-1441-2017, 2017.

Westermann, S., Barboux, C., Bartsch, A., Delaloye, R., Grosse, G., Heim, B., Hugelius, G., Irrgang, A., Kääb, A. M., Matthes, H., Miesner, F., Nitze, I., Pellet, C., Seifert, F. M., Strozzi, T., Wegmüller, U., Wieczorek, M., and Wiesmann, A.: ESA Permafrost Climate Change Initiative (Permafrost_cci): Permafrost extent for the Northern Hemisphere, v5.0, https://doi.org/10.5285/D235665772EC4B558E9A89AC85595E71, 2025.

Widhalm, B., Bartsch, A., Strozzi, T., Jones, N., Khomutov, A., Babkina, E., Leibman, M., Khairullin, R., Göckede, M., Bergstedt, H., von Baeckmann, C., and Muri, X.: InSAR-derived seasonal subsidence reflects spatial soil moisture patterns in Arctic lowland permafrost regions, The Cryosphere, 19, 1103–1133, https://doi.org/10.5194/tc-19-1103-2025, 2025.

https://doi.org/10.5194/egusphere-2026-5477
Preprint. Discussion started: 22 September 2026

Zink, M. and Moreira, A.: TanDEM-X mission status: The new topography of the earth takes shape, 2014 IEEE Geoscience and Remote Sensing Symposium, 3386–3389, https://doi.org/10.1109/igarss.2014.6947207, 2014.

Zwieback, S., Liu, L., Rouyet, L., Short, N., and Strozzi, T.: Advances in InSAR Analysis of Permafrost Terrain, Permafrost & Periglacial, 35, 544–556, https://doi.org/10.1002/ppp.2248, 2024.